Supporting Information

High strength hydrogels enable dendrite-free Zn metal anodes and high-capacity Zn-MnO_2 batteries via a modified mechanical suppression effect

Ruijie Zhu, Huijun Yang, Wei Cui, Laras Fadillah, Tianhong Huang, Zetao Xiong, Chunmei Tang, Damian Kowalski, Sho Kitano, Chunyu Zhu, Daniel R. King*, Takayuki Kurokawa, Yoshitaka Aoki, and Hiroki Habazaki,*

Prof. C. Zhu
School of Electrical and Power Engineering, China University of Mining and Technology, Xuzhou 221116, China
E-mail: zcyls@cumt.edu.cn

R. Zhu, Dr. L. Fadillah, Z. Xiong, C. Tang, Dr. S. Kitano, Prof. Y. Aoki, Prof. H. Habazaki.
Graduate School of Chemical Sciences and Engineering, Hokkaido University, Sapporo, Hokkaido 060-8628, Japan

Dr. H. Yang
National Institute of Advanced Industrial Science and Technology (AIST), 1-1-1, Umezono, Tsukuba 305-8568 Japan.

Dr. W. Cui, Prof. D. R. King, Prof. Takayuki Kurokawa
Faculty of Advanced Life Science, Hokkaido University, Sapporo 001-0021, Japan.
E-mail: dking@sci.hokudai.ac.jp

T. Huang
Department of Mathematics, University of Wisconsin Madison, Madison, WI, USA 53705

Prof. D. Kowalski
Faculty of Chemistry and Biological and Chemical Research Centre, University of Warsaw, Zwirki i Wigury 101, 02-089 Warsaw, Poland.

Prof. S. Kitano, Prof. D. Kowalski, Prof. Y. Aoki, Prof. H. Habazaki.
Division of Applied Chemistry, Faculty of Engineering, Hokkaido University, Sapporo, Hokkaido 060-8628, Japan
Correspondence to zcyls@cumt.edu.cn (C. Zhu)
dking@sci.hokudai.ac.jp (D. R. King)

1. Supplemental experiments

***1.1 Mechanical properties measurements*:** Uniaxial tensile tests were performed on all the prepared hydrogels at the maximum water content. A tensile-compressive tester (INSTRON 5965, Instron Co.) was used to conduct the tensile tests. All of the dumbbell shaped samples (length of 12 mm, width of 2 mm, the thickness range is 2-3 mm depending on the sample) were stretched along the length direction at an extension rate of 100 mm min^{-1}.

Uniaxial compress tests were performed by using a compressive tester (Tensilon RTC-1310A, Orientec Co). Samples were firstly cut to a disk shape with a diameter of 10 mm before test. The compression rate was set to 0.1x mm min^{-1}, where the x is the thickness of the sample.

1.2 GITT tests for the DNGF separated Zn || MnO_2 cell: The GITT test for high-capacity Zn || MnO_2 cell was conducted by intermittently charging (or discharging) the cell until the cell voltage reached the cut-off voltage. Here, the Zn || MnO_2 cell was firstly discharged at a current density of 308 mA g^{-1} for 60 s, which was defined as one section. Then the cell would rest for 120 min for the completion of ion-diffusion. Once the cell voltage achieved the cut-off voltage of 0.8 V, the GITT test would be stopped. The capacity of GITT discharge was the sum of the capacities of all discharge sections.

***1.3 Additional electrochemical measurements*:** Cyclic voltammetry (CV) and Electrochemical impedance spectra (EIS) was measured on an electrochemistry workstation (Princeton, VersaSTAT3). For Zn || MnO_2 cells, potentiostatic EIS measurements were conducted at a controlled voltage of 1.35 V (vs. Zn/Zn^{2+}), and the frequency range was 100 kHz to 0.1 Hz. Ionic conductivities of GPEs were calculated through EIS measurements. For GPEs, the hydrogel ionic conductor was sandwiched between two stainless steel disks with the same dimension. For the pure electrolyte, an O-ring was sandwiched between two stainless steel disks. The ionic conductivity of different samples was calculated by ohmic resistance. The ionic conductivity σ was obtained by:

$$\sigma = l/RA \qquad (Eq\ S1)$$

where l is the thickness of the sample, R is the ohmic resistance, and A is the geometric surface area of the sample, respectively.

***1.4 Simulation details*:**

1.4.1 Simulation of the capacitive current:

The total stored charge during a CV test was separated into these components: i) Faradaic contribution from the ion-insertion process; ii) Faradaic contribution from the

charge-transfer process with surface atoms, namely the pseudocapacitance; iii) Nonfaradaic contribution from the electrical double-layer capacitance.[1] Here, the current that was contributed by pseudocapacitance and the double-layer capacitance were evaluated by:

$$I = av^b \qquad (Eq\ S2)$$

Where i is the current and v is the sweep rate, a is an adjustable parameter, b is the slope of the plot of log i vs log v. Eq. S2 can be modified to the following form in a separated CV cycle:

$$I(V)/v^{0.5} = k_1v^{0.5}+k_2 \qquad (Eq\ S3)$$

where $I(V)$ is the measured current at a specific voltage during a single CV cycle, k_1 and k_2 are two parameters that can be obtained by linear fitting every $I(V)/v^{0.5}$ and $v^{0.5}$. The product of k_1 and v (the result is current) is regarded as the contribution from pseudocapacity. By drawing a plot of k_1v and V, figure of the capacitive current can be obtained.

1.4.2 Simulation of the Zn plating process:

To simulate the process of Zn deposition during a galvanizing test in a Swagelok cell, a three-dimensional (3D) model was employed. As we depicted in Figure S15, electrochemical models were built by using COMSOL Multiphysics with the “2D-

Tertiary Current Distribution" interface. The geometric model included 3 parts: a cell chamber (the largest cuboid shown in Figure S15), a cathode zone (the red cuboid) and a certain number of ellipsoids. The height of the cathode zone is high enough to avoid the coating height break through the cathode zone during galvanizing. The surface of the ellipsoids above the anode surface was all used as active sites for galvanizing, and the electrolyte was filled with the entire battery chamber by default. The entire battery is electrically neutral in the 1D direction through the Nernst-Planck-Poisson equation. The relationship between electrode reaction and overpotential is described by the Butler-Volmer equation. The simulation of galvanizing under different conditions was realized by adjusting the parameters. The relationship between electrode reaction and overpotential is described by the Butler-Volmer equation. The simulation of galvanizing under different conditions were realized by adjusting the parameters. Potential of the electrolyte was obtained by combining the following relationship:

$$i_l = -\sigma_l \nabla E_l \quad \textit{(Eq S4)}$$

$$\nabla \cdot i_l = 0 \quad \textit{(Eq S5)}$$

Where i_l is the current density of electrolyte (vector), σ_l is the ionic conductivity of the electrolyte and E_l is the potential of electrolyte.

The Butler-Volmer equation was used to express the electrode reaction under dynamic conditions:

$$j_{loc} = j_0(\exp(\frac{\alpha_a F\eta}{RT} - \exp(\frac{-\alpha_c F\eta}{RT}) \qquad (Eq\ S6)$$

where j_{loc} is the local current density, j_0 is the exchange current density, η is the overpotential, α_a is the anodic transfer coefficient while α_c is the cathodic transfer coefficient, respectively.

Thickness of the Zn coating was calculated by Faraday's laws of electrolysis:

$$V = \frac{i_{loc} t M_{Zn}}{2F\rho_{Zn}} \qquad (Eq\ S7)$$

where t is the deposition time, M_{Zn} is the molar mass of Zn, ρ_{Zn} is the mass density of Zn while V is the volume of deposited Zn for a small area, respectively.

The parameters are summarized in Table S5.

2. Supplemental Figures

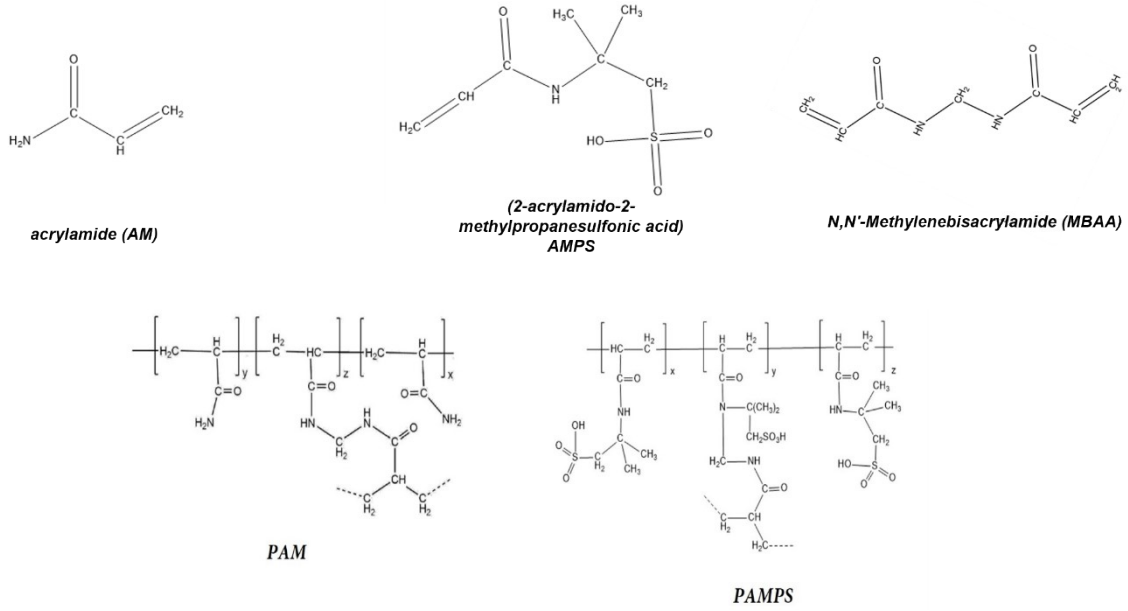

Figure S1 Chemical structure of the AM, AMPS, MBAA, PAMPS and PAM.

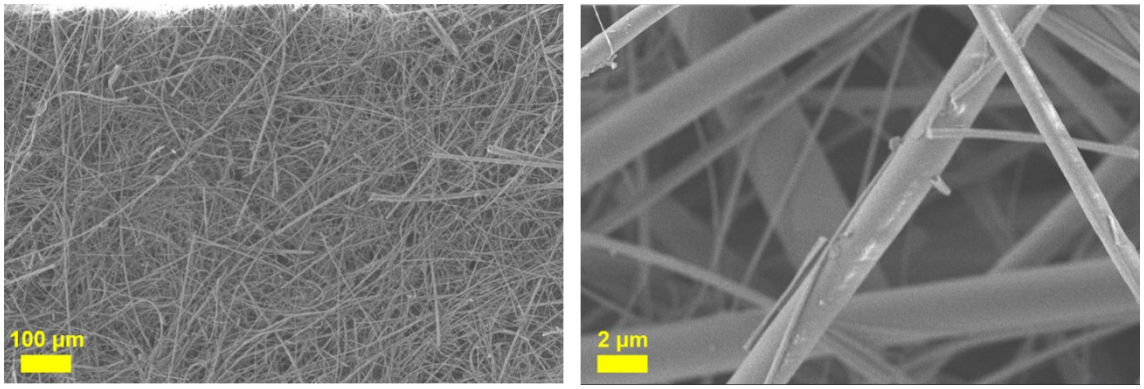

Figure S2 SEM images of the used glass fiber.

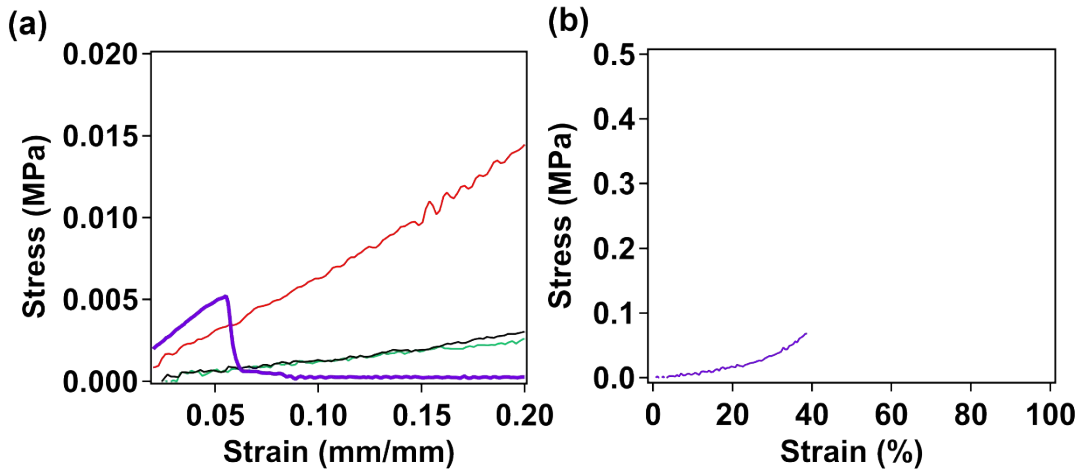

Figure S3 Enlarged view of the loading curves of different gels under (a) uniaxial elongation and (b) uniaxial compression, the figure corresponds to Figure 1 in the manuscript.

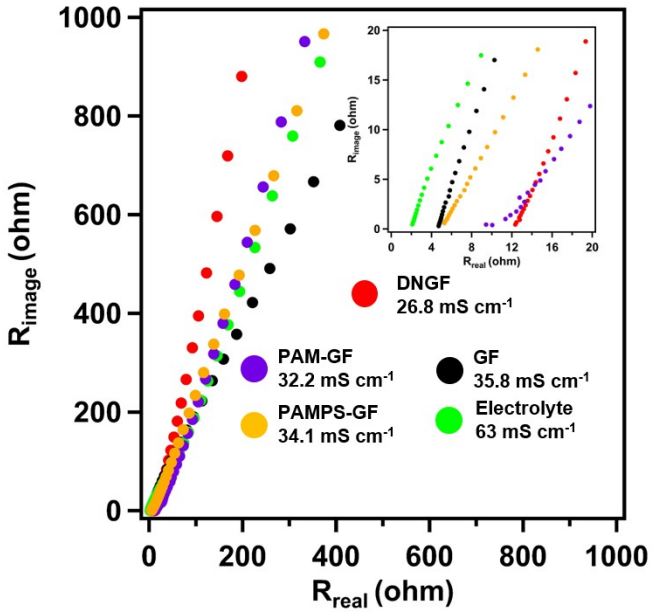

Figure S4 Nyquist plots of different separators (hydrogel electrolytes).

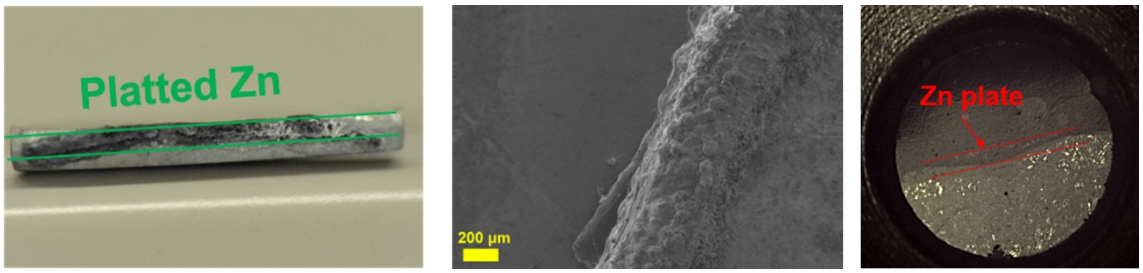

Figure S5 Optical photo (left) and SEM image (mid) and a zoom in view (right) of the Zn electrode corresponding to in-situ optical observation.

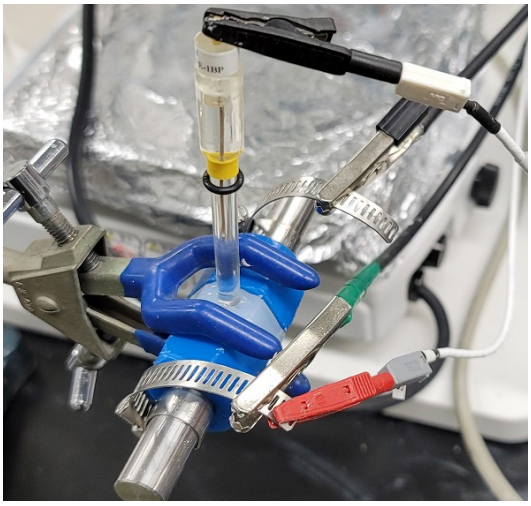

Figure S6 Optical photo of the three-electrode quasi-solid-state cell. An Ag/AgCl reference electrode was set in a drilled hole and touched with the added liquid electrolyte.

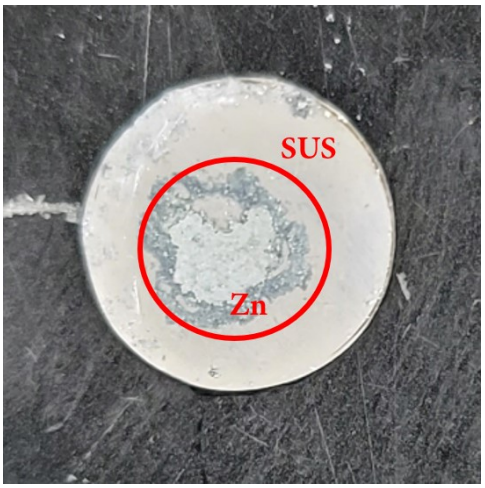

Figure S7 Optical photo of the Zn electrode on the stripping side in the potentiostatic Zn deposition test. The substrate is a stainless-steel case (SUS316). When the Zn electrode was stripped to such a condition, the open circuit voltage (OCV) of the cell in a two-electrode cell is generally several hundred milli-volt. Obviously, it is impossible to realize potentiostatic Zn plating test in a two-electrode cell.

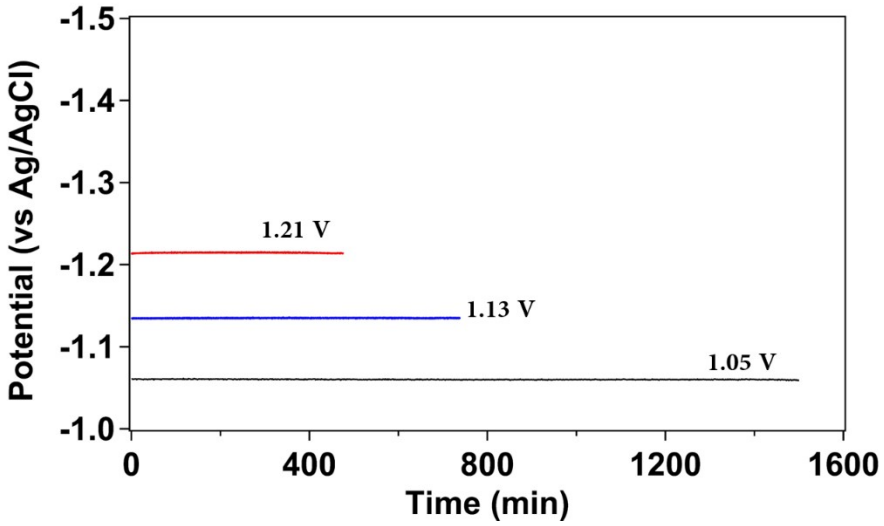

Figure S8 Voltage profiles corresponding to the potentiostatic Zn deposition tests**.**

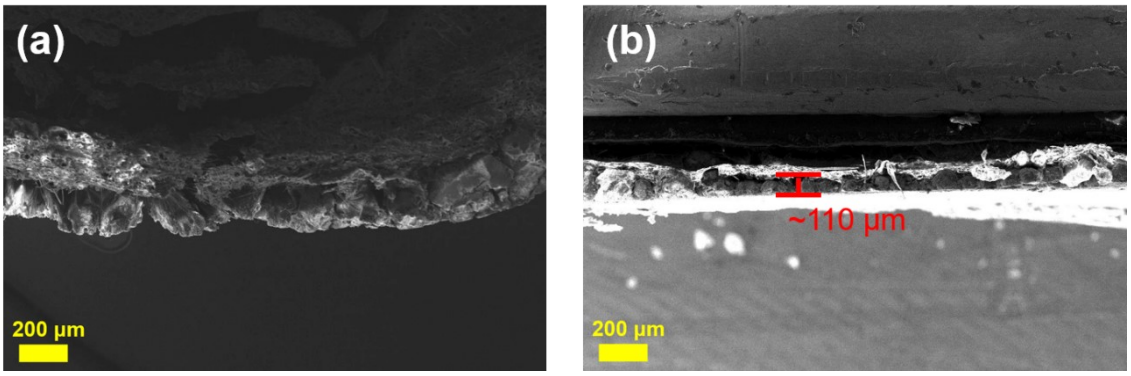

Figure S9 SEM images of the a) DNGF and the b) Zn electrode after the potentiostatic deposition test. The observed samples are corresponding to -1.05 V deposition condition.

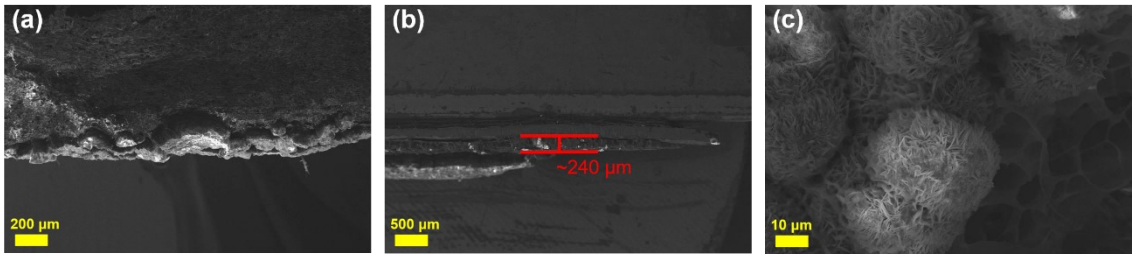

Figure S10 SEM images of the a) DNGF and the b,c) Zn electrode in the potentiostatic deposition test. The observed samples are corresponding to -1.21 V deposition condition.

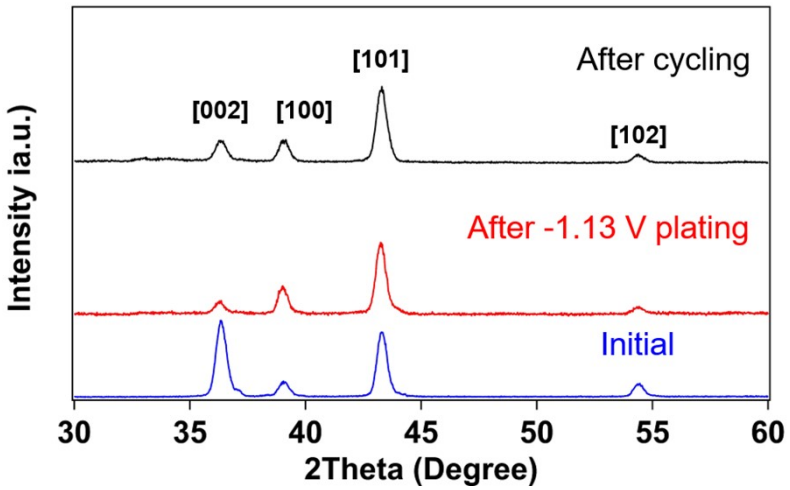

Figure S11 In-plane XRD pattern of Zn electrodes before treatment (blue), after potentiostatic (red) and after 1000 cycle (5 mA cm^{-2}, 2.5 mA h cm^{-2}).

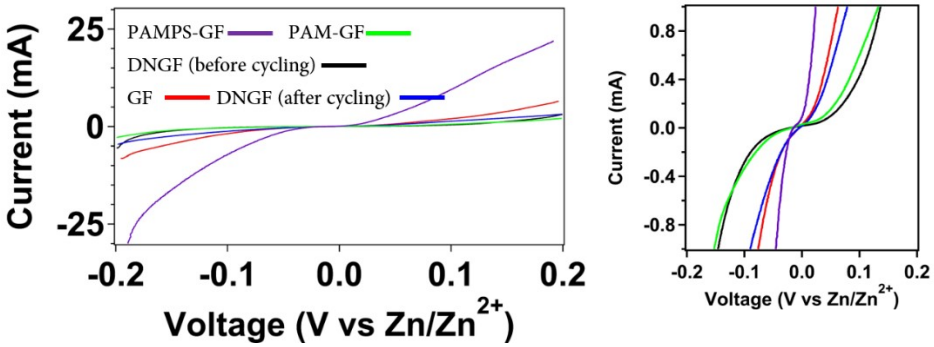

Figure S12 Linear sweep voltammetry (LSV) of Zn || Zn symmetric cells with different separators. The voltage range is from -0.2 V to 0.2 V (vs Zn/Zn^{2+}), scan rate is 1 mV s^{-1}.

Exchange current density of Zn plating/stripping that can be obtained from this LSV measurement is a great discrepancy from the normal value. This is because of the severe concentration polarization and the significant asymmetry factors in the two-electrode system.

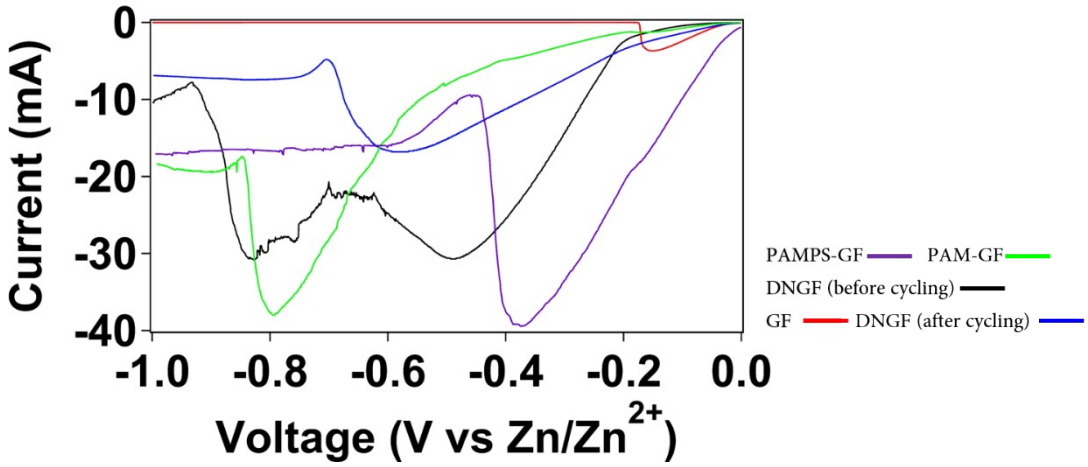

Figure S13 Linear sweep voltammetry (LSV) of Zn || Zn symmetric cells with different separators. The voltage range is -1V to 0 V (vs Zn/Zn^{2+}), the scan rate is 1 mV s^{-1}. The intense change of current at high voltage is ascribed to that the concentration field inside the cell is difficult to achieve equilibrium.

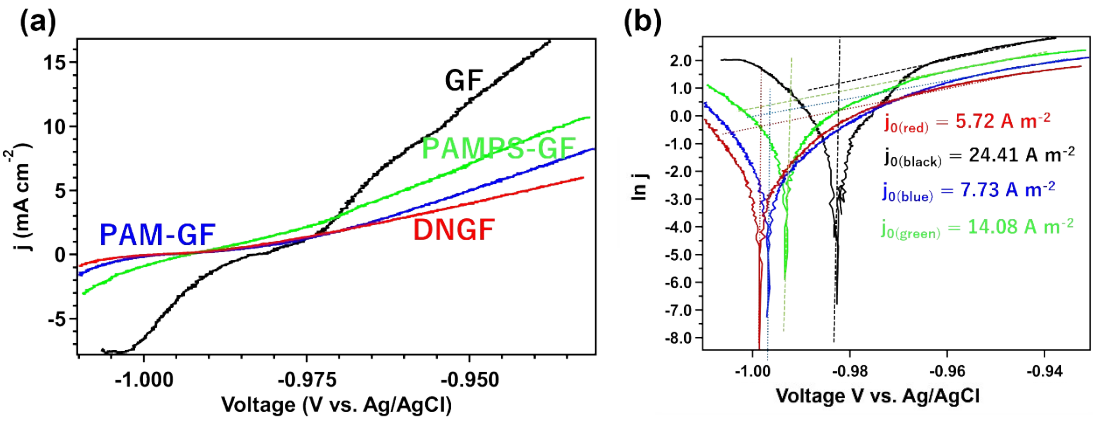

Figure S14 (a) Linear sweep voltammetry (LSV) of Zn || Zn symmetric cells with different separators (tested in the three-electrode Swagelok cell). The voltage range is -1.01 V to -0.93 V (vs Ag/AgCl) and the scan rate is 1 mV s^{-1}. (b) The Tafel plots that

correspond to the LSV tests. The exchange current density is obtained by assuming the anodic transfer coefficient α_a (in the Butler-Volmer equation) is equal to the cathodic transfer coefficient α_c.

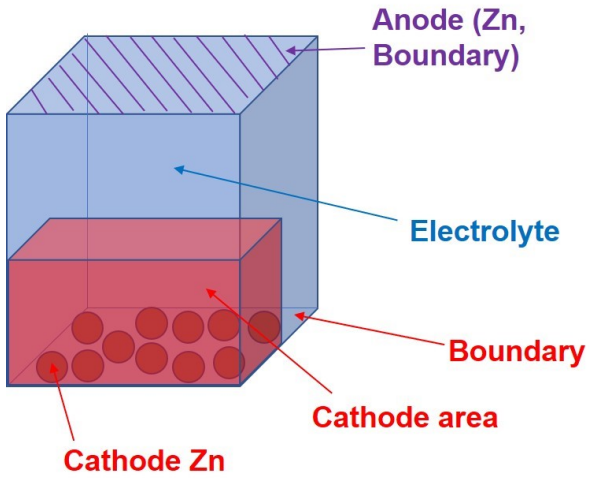

Figure S15. Geometric model for the simulation of Zn plating.

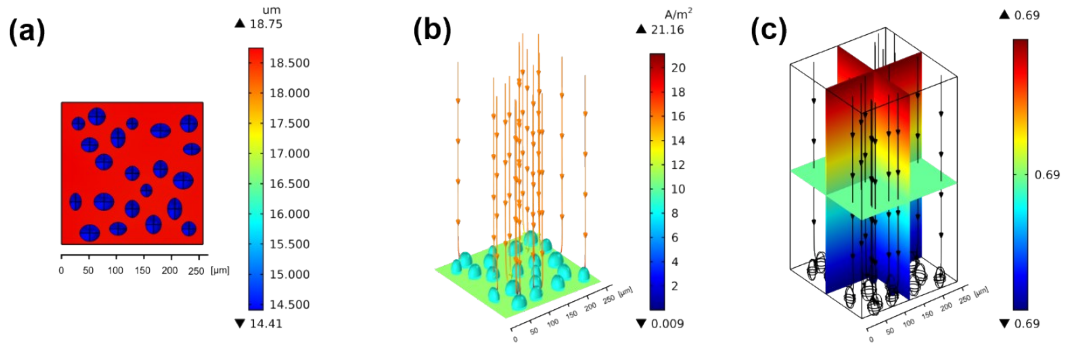

Figure S16. Simulation results of the a) thickness change, b) current field and c) potential distribution in a DNGF separated Zn || Zn cell. Here, the applied current density was distributed according to the area ratio of red area (Zn plate) and blue area (newly deposited Zn crystals). The exchange current density of the red area is $j_{0(no\ separator)}$ and the blue is $j_{0(DNGF)}$. It could be seen that the thickness of the Zn coating on the substrate would

be higher than those on the newly deposited crystals. This shows that when the spherical crystal is subjected to the mechanical suppression effect, the deposition of Zn on the whole electrode would become more uniform.

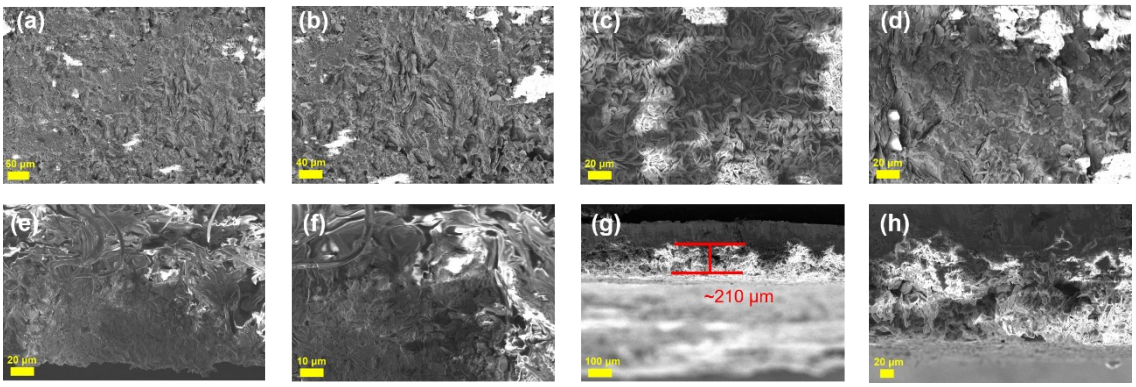

Figure S17 SEM images of the as cycled electrodes.

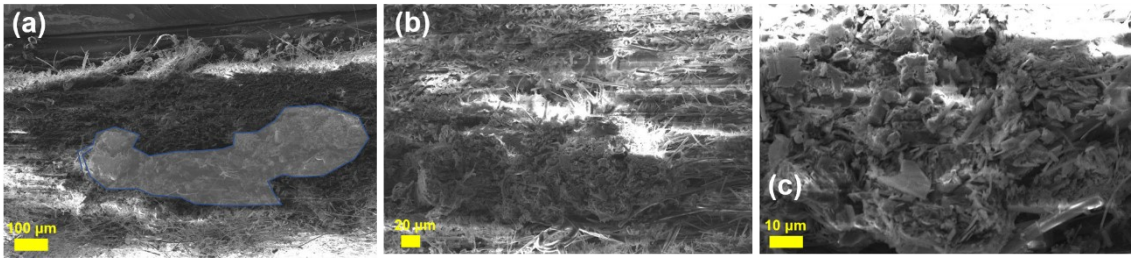

Figure S18 a, b, c) SEM images of PAMPS-GF after cycling in the symmetric cell (1 mA cm^{-2}, 1 mA h cm^{-2}). The Zn crystal grew inside the PAMPS-GF (marked area), leading to the short-circuit.

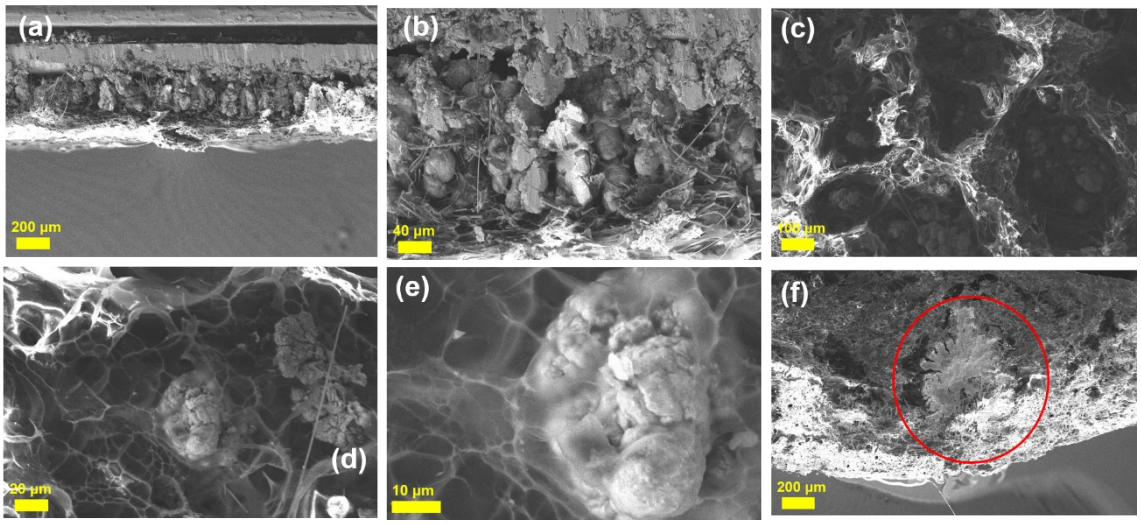

Figure S19 SEM images of the components from the PAM-GF separated symmetric cell after cycling. a, b) Cross-sectional observation of the Zn electrode. c, d, e) Direct observation of PAM-GF after freeze-drying. f) Cross-sectional observation of the PAM-GF separator.

As shown in Fig. S18f, The Zn crystal grew vertically inside the PAM-GF, finally causing the short-circuit. The spherical Zn crystals have the capability to break the gel framework (Fig. S18d,e), indicating the mechanical strength of PAM-GF is not high enough to stop the growth of Zn dendrites.

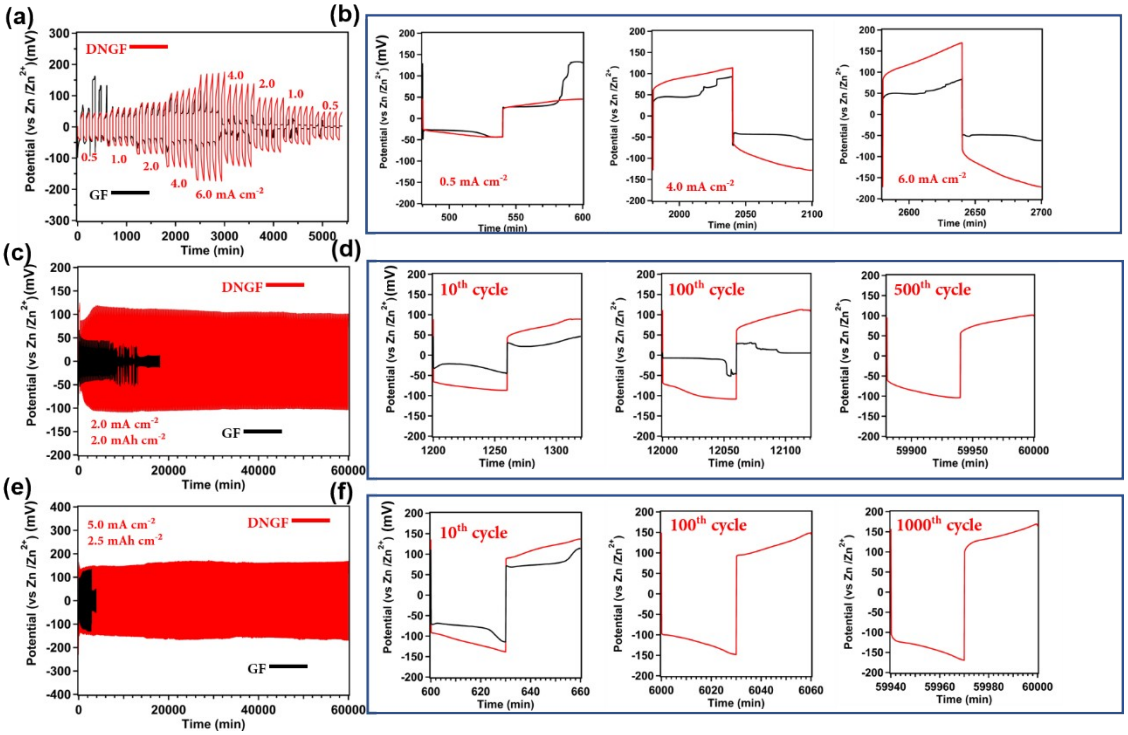

Figure S20 Performance of symmetric cells tested at a, b) 0.5 mA cm^{-2} to 6.0 mA cm^{-2}, c, d) 2.0 mA cm^{-2} with a capacity of 2 mA h cm^{-2} and e,f) 5 mA cm^{-2} with a capacity of 2.5 mA h cm^{-2}. Red lines refer to cells that used DNGF as a separator and electrolyte, and black lines refer to cells that used glass fiber separator. Cells that were separated by DNGF were finally stopped manually in order to make way for other tests.

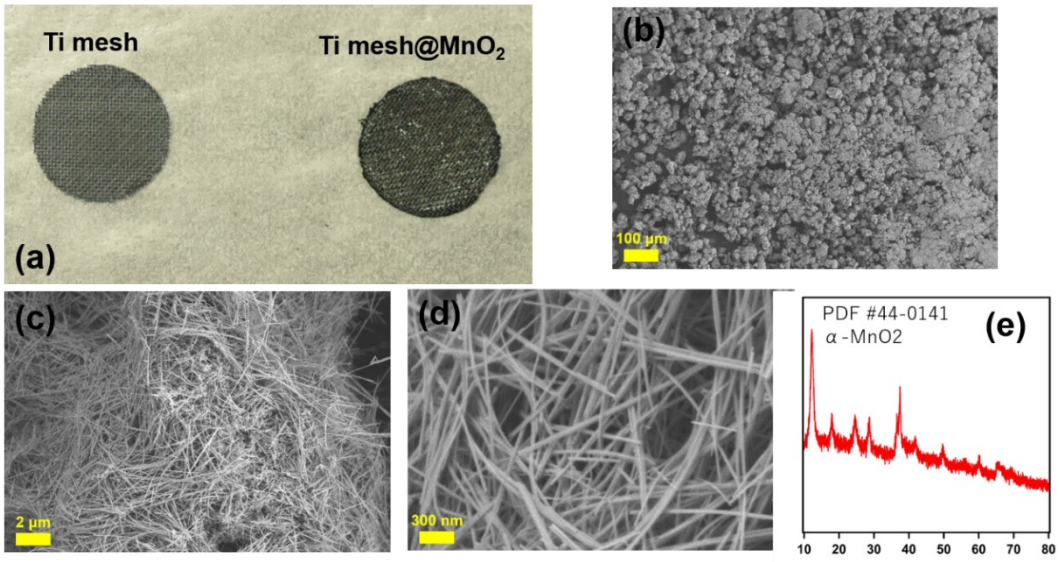

Figure S21 Characterization of the cathode material. a) Optical photos of the Ti mesh and the MnO_2 cathode. b, c, d) SEM images of the α-MnO_2 nanowires. e) XRD pattern of the α-MnO_2 nanowires**.**

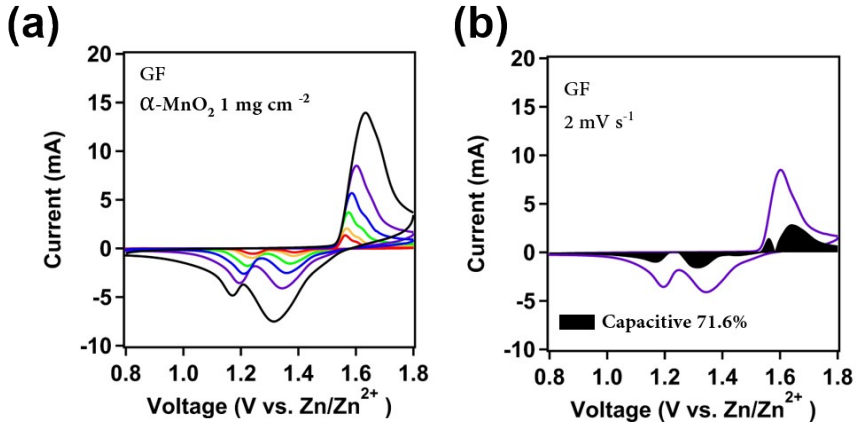

Figure S22 a) Cyclic voltammetry of the low-capacity Zn || MnO_2 battery using glass fiber as a separator. b) Capacitive contribution of glass fiber separated Zn || MnO_2 battery to the total charge storage at 2 mV s^{-1}.

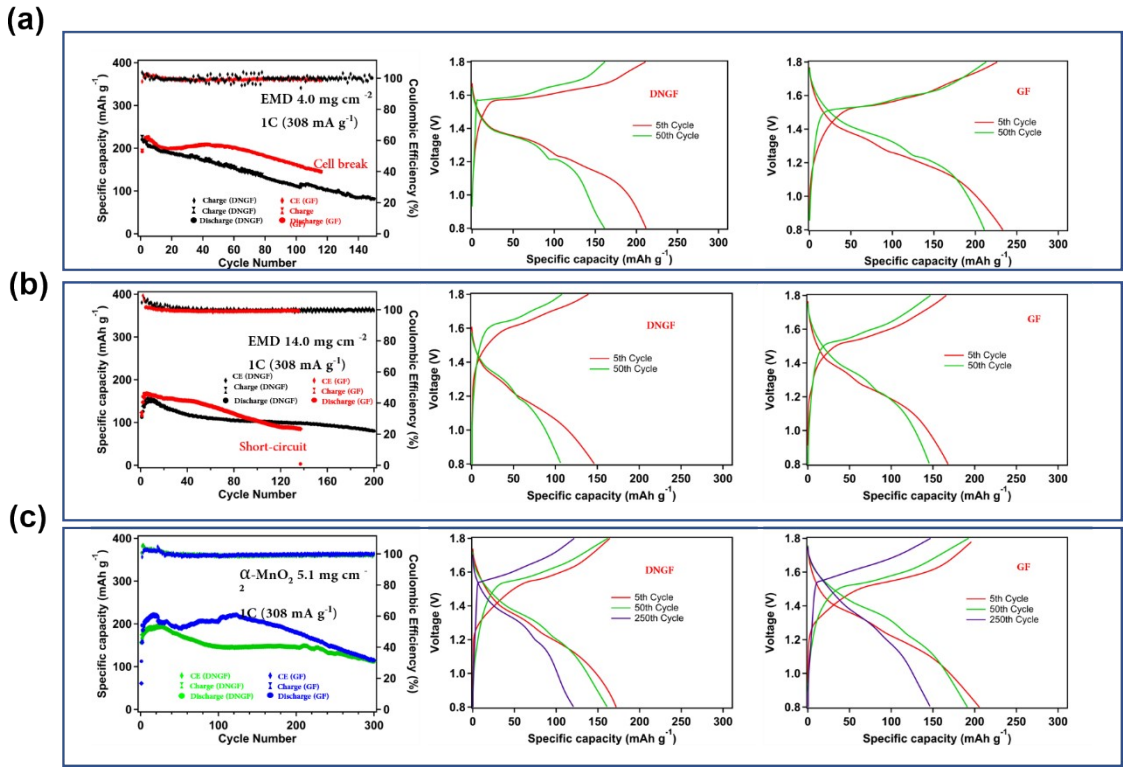

Figure S23 a, b) Charge/discharge performance of Zn || MnO_2 batteries using commercial electrolytic manganese dioxide (EMD). Here, the left figure is cyclic performance of the batteries, where red points stand for batteries that used glass fiber as separator and black points stand for batteries that used DNGF.

c) Charge/discharge performance of Zn || MnO_2 batteries using an α-MnO_2 cathode. Here, the left figure is the cyclic stability of the batteries where blue points stand for the batteries that use glass fiber as separators and black points stand for the batteries that uses DNGF.

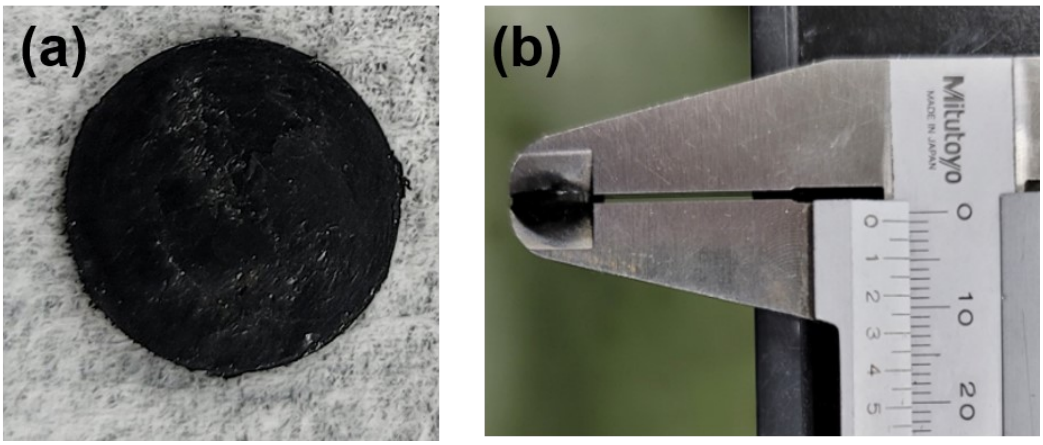

Figure S24 a, b) Optical photos of the high-capacity MnO_2 cathode. Thickness of the cathode is around 1 mm.

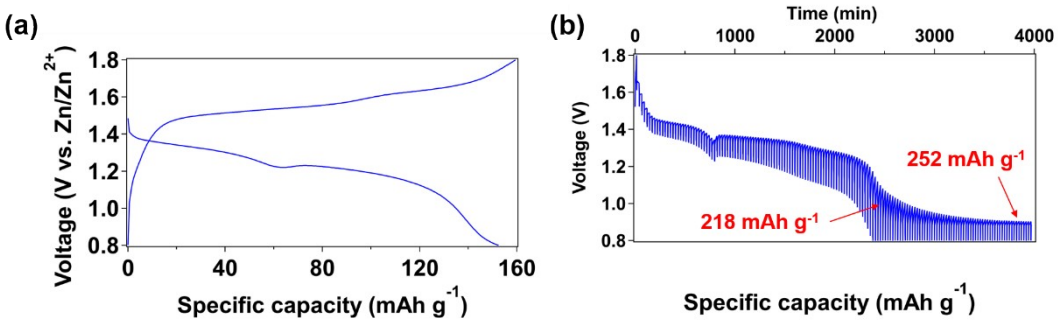

Figure S25 (a) Voltage profile of an additionally prepared Zn||MnO_2 cell with HCM cathode at 4th cycle. (b) GITT result of the Zn||MnO_2 cell after 4 cycles.

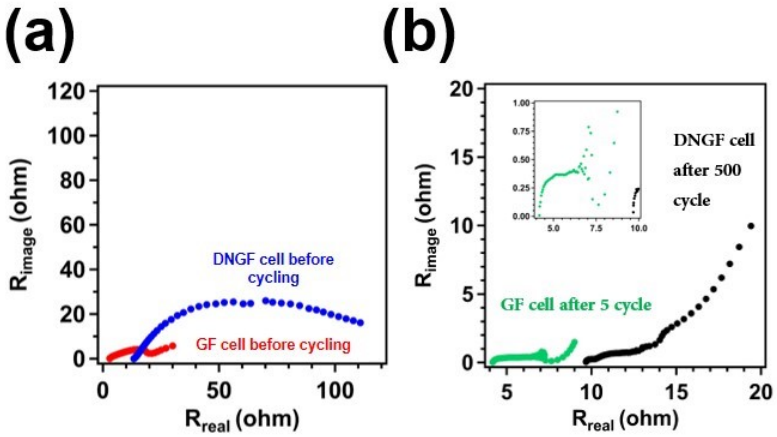

Figure S26 Nyquist plot of high-capacity Zn || MnO_2 batteries a) before and b) after cycling. This is consistent with our results that were obtained from low-capacity Zn || MnO_2 cells.

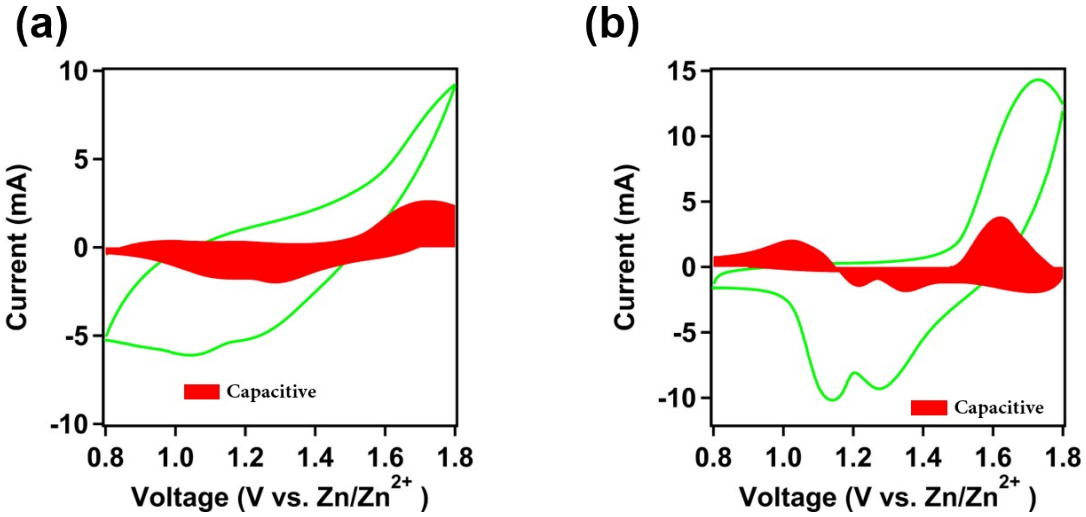

Figure S27 Capacitive contribution of DNGF separated Zn || MnO_2 battery to the total charge storage at 1 mV s^{-1} a) before and b) after cycling. Obviously, the simulated contribution is not reliable because the simulated capacitive current is higher than the real

total current. This phenomenon is likely attributed to the electrode reactions being non-uniform in the high-capacity cathode. In the depths of the cathode, the reaction exhibited a serious hysteresis due to the concentration polarization.

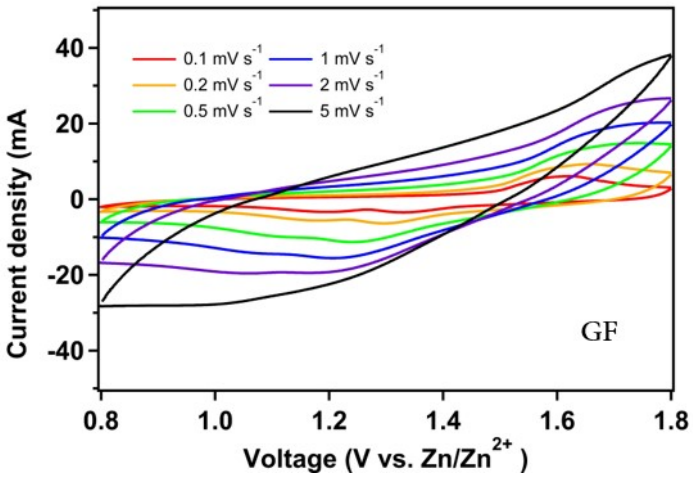

Figure S28 Cyclic voltammetry curve of the glass fiber separated high-capacity Zn || MnO_2 battery.

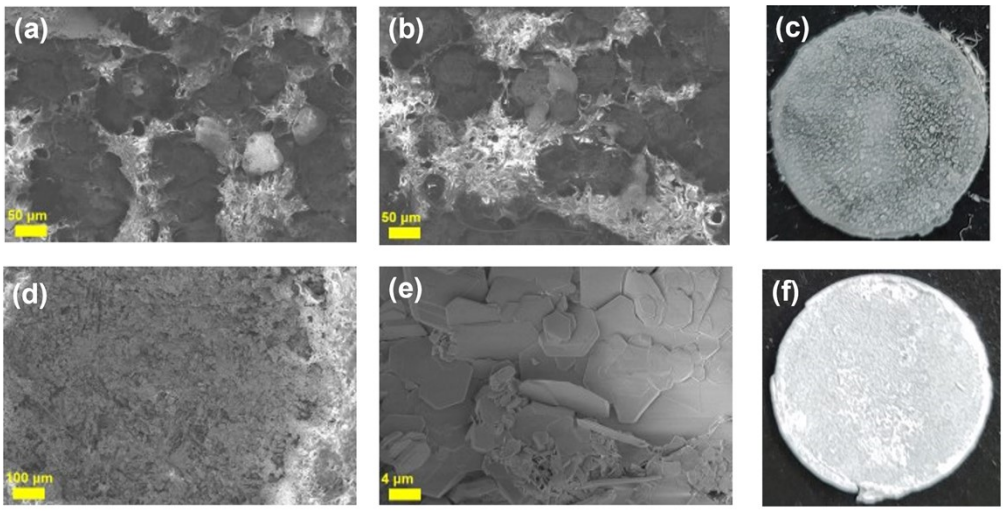

Figure S29 a, b) SEM images and c) an optical photo of the PAM-GF protected Zn foil after the potentiostatic plating test (voltage of -1.05 V (vs. Ag/AgCl)). d, e) SEM images and f) an optical photo of the PAM-GF protected Zn foil after the symmetric cell tests. (Corresponding to Figure S20).

For PAM-GF, it is also able to seed uniform Zn crystals, thereby alleviating the growth of Zn dendrites, but its ability is not as strong as the DNGF. To achieve dendrite-free Zn metal anodes, we believe that the design of GPEs for aqueous ZIBs should mainly focus on the optimization of the mechanical properties of the prepared GPEs**.**

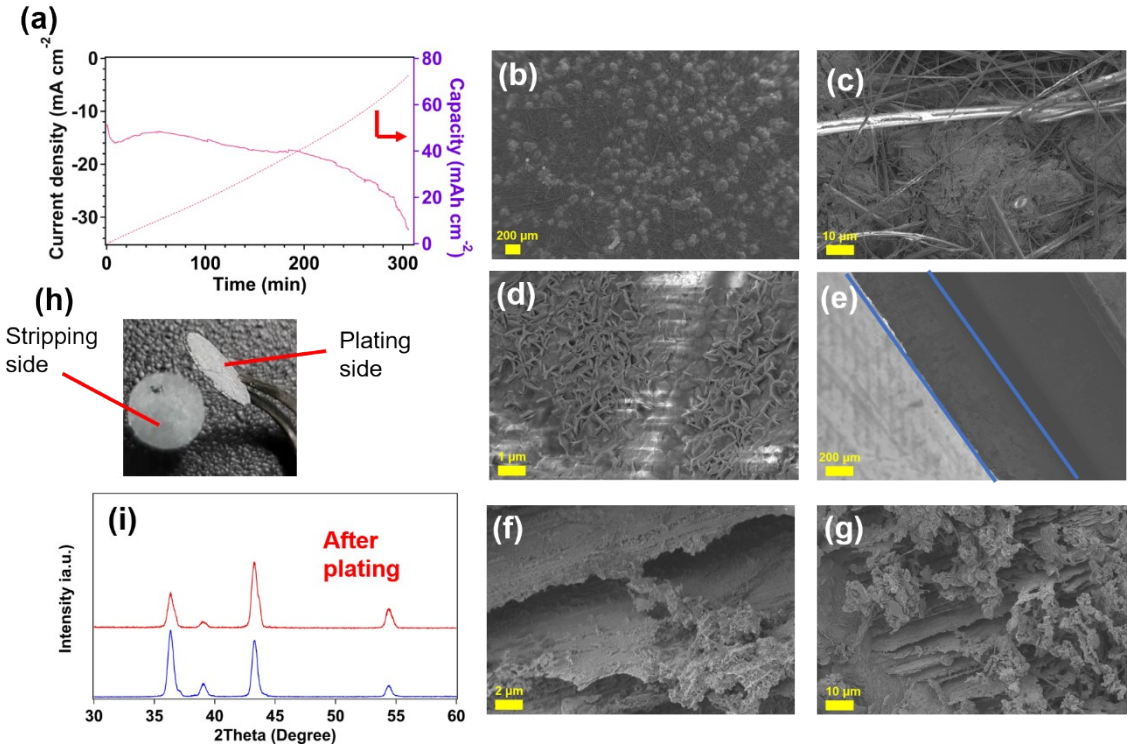

Figure S30 Results of the potentiostatic plating test for glass fiber separator. a) Current profiles of Zn deposition using GF separator at constant voltage of -1.05 V (vs. Ag/AgCl). SEM images of the corresponded Zn plate electrodes. b-e) the galvanized Zn electrode, f, g) Zn stripped Zn electrode. h) Optical photo of the corresponded Zn disk electrodes. j) In-plane XRD patterns of the Zn electrode before (blue) and after plating (red).

This result shows even when the conventional glass fiber is used as the separator, the deposition of Zn still can be uniform occasionally. The interpretation for this result is shown in Figure S31.

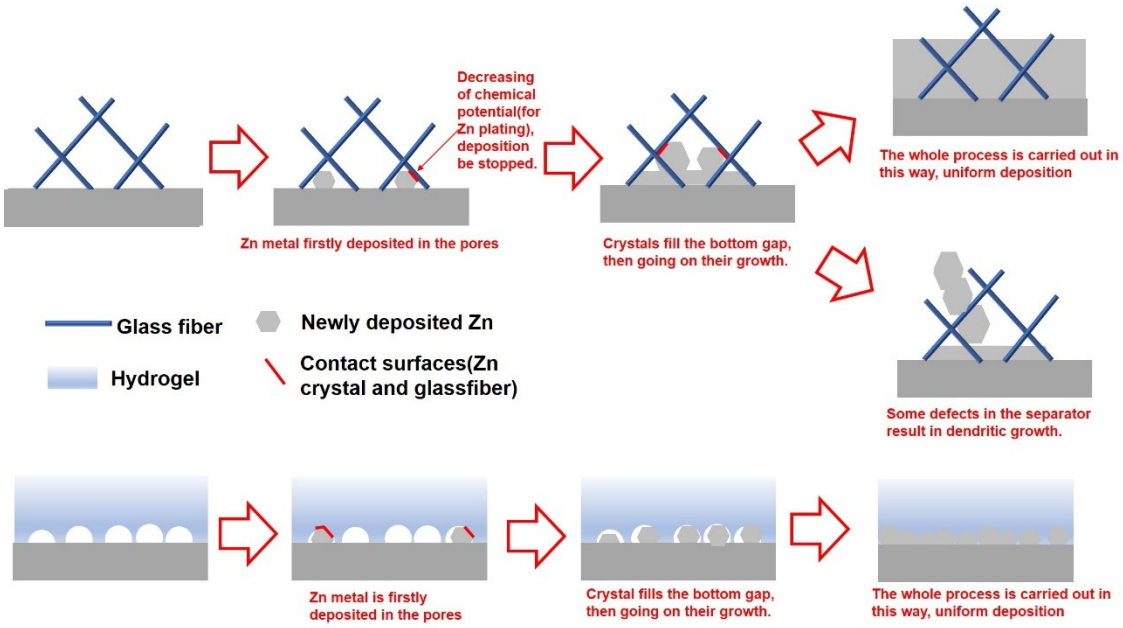

Figure S31 Schematic illustration for the possible mechanical suppression effect at different conditions.

As shown in Figure S31 (top), for the conventional porous separator, e.g. glass fiber, the deposition of Zn may exhibit two different states. Zn crystals are firstly formed in the pores of the separator. Once the separator framework can make effective contact with the Zn crystals, the growth of Zn dendrites will be suppressed. Otherwise, Zn dendrites will grow along the defect (pores) in the separator.

For GPEs, due to their good structural uniformity, Zn dendrites cannot grow unimpededly, unless the additional electrochemical potential allows dendrites to break the polymer framework.

The above-mentioned phenomena and discussions show us new inspiration for designing

a new type of separator. If a porous separator can have both good mechanical strength and evenly distributed pores, it will be able to inhibit the growth of Zn dendrites without increasing of the plating overpotential.

Table S1. Physical parameters of the GPEs used in this work.

Sample	Weight before swelling (mg)	Weight after swelling (mg)	Swelling ratio (mL g^{-1}) [a]	Shear modulus (kPa) [b]
DNGF	29.8	240.9	7.1	94.2
PAM-GF	24.5	253.2	9.3	8.6
PAMPS-GF	13.6	172.3	11.7	-
PAM	11.6	146.8	11.6	3.2

a) The swelling ratio is calculated through the equation: $q=V_a/W_0$

where V_a is the volume of the absorbed water at equilibrium, W_0 is the weight of the dried hydrogel.

b) The shear modulus is estimated by an empirical method, assuming a Poisson's ratio of 0.5: G=E/3

where G is the shear modulus and E is the Young's modulus (calculated by tensile testing).

Table S2. Comparing Young's modulus of different GPEs used in RAZIBs.

GPEs	Young's Modulus (kPa)	Ref.
EG-waPUA	8.06*	2
PAM GPE		
Zwitterionic ZSC GPE	15.31*	3
PAM	14.29*	3
PVAA-GO**	12.90*	4
PVA**	8.69*	4
PAMPS-K30-MC2.0**	32.22*	5
DNGF	282.6	This work

* The value is calculated from the results of tensile tests shown in the paper.

** This gel was used in an alkaline Zn-air battery.

Table S3. Performance comparison of different GPEs modified RAZIBs

GPEs	Symmetric Cell		Zn || MnO_2			Ref
	Current Density Capacity	Cycles	m(MnO_2)	(Dis)charge rate	Cycles/ Retention(%)	
PAM	- mA cm^{-2} - mAh cm^{-2}	-	2.5 mg cm^{-2}	2000 mA g^{-1}	500 /98.5	6
HPE GPE [a]	- mA cm^{-2} - mAh cm^{-2}	-	1.0-2.5 mg cm^{-2}	500 mA g^{-1}	1000 /97	7
EG-waPUA PAM GPE	- mA cm^{-2} - mAh cm^{-2}	-	1.0-2.5 mg cm^{-2}	800 mA g^{-1}	600 /88.4	2
Pluronic hydrogel electrolyte	- mA cm^{-2} - mAh cm^{-2}		- mg cm^{-2} [c]	60 mA g^{-1}	300 /83	8
Zwitterionic ZSC GPE	0.5 mA cm^{-2} 0.5 mAh cm^{-2}	200	1.0-2.5 mg cm^{-2} 1 mAh cm^{-2}	2000 mA g^{-1}	1200 /90.4	3
PZHE-SBMA	0.5 mA cm^{-2} 0.25 mAh cm^{-2}	7000	4-5 mg cm^{-2}	1000 mA g^{-1}	500 /83	14 [b]
DNGF GPE	**5 mA cm^{-2}** **2.5 mAh cm^{-2}**	**>1000**	**30 mg cm^{-2}**	**308 mA g^{-1}**	**500**	This study
DNGF GPE	**1 mA cm^{-2}** **1 mAh cm^{-2}**	**>1000**	**1 mg cm^{-2}**	**3080** mA g^{-1}	**9500**	This study

a HPE consists of gelatin, PAM and PAN fiber.

b The used cathode material is VS_2.

Table S4. Performance comparison of RAZIBs that are modified by different materials

Materials	Symmetric Cell		Zn || MnO_2			Ref
	Current Density Capacity	Cycles	m(MnO_2)	(Dis)charge rate	Cycles/ Retention(%)	
MOF-PVDF Separator [a]	1 mA cm^{-2} 0.5 mAh cm^{-2}	500	1.6 mg cm^{-2}	308 mA g^{-1}	50	9
MOF-PVDF Separator [b]	0.5 mA cm^{-2} 0.5 mAh cm^{-2}	1500	4.2 mg cm^{-2}	500 mA g^{-1}	180 /94.4	10
PA protective layer	10 mA cm^{-2} 10 mAh cm^{-2}	35	1.3 mg cm^{-2}	616 mA g^{-1}	1000 /88	11
			15 mg cm^{-2}	616 mA g^{-1}	1000	
ZrO_2 protective layer	0.25 mA cm^{-2} 0.125 mAh cm^{-2}	3800	- mg cm^{-2}	1000 mA g^{-1}	3000 /92.3	12c
ZnS protective layer	2 mA cm^{-2} 2 mAh cm^{-2}	600	< 7 mg cm^{-2} [d]	1500 mA g^{-1}	2500 /87.6	13
In based protective layer	0.25 mA cm^{-2} 0.05 mAh cm^{-2}	3500	0.8 mg cm^{-2}	1500 mA g^{-1}	400 /72	15
DNGF GPE	**5 mA cm^{-2} 2.5 mAh cm^{-2}**	**>1000**	**30 mg cm^{-2}**	**308 mA g^{-1}**	**500 /40**	**This study**
DNGF GPE	**1 mA cm^{-2} 1 mAh cm^{-2}**	**>1000**	**1 mg cm^{-2}**	**3080 mA g^{-1}**	**9500 /50**	**This study**

[a] The MOF used is Universistetet I Oslo-66.

[b] The MOF used is zeolitic imidazolate framework 7 (ZIF-7).

[c] The cathode used is V_2O_5.

[d] Since the author did not mention the mass-loading of the MnO_2 cathode, this value is speculated based on their anode capacity.

Table S5. Parameters that were used in multi-physics simulation.

Parameter	Value	Ref.
$E^{\varphi}_{Zn/Zn2+}$	-0.76 V	-
$j_{0\ (no\ separator)}$	24.41 A m^{-2}	Experimental
$j_{0\ (DNGF)}$	5.42 A m^{-2}	Experimental
j	1 mA cm^{-2}	Experimental
M_{Zn}	65 g mol^{-1}	-
ρ_{Zn}	7140 kg m^{-3}	-
$\sigma_{(DNGF)}$	26.8 mS cm^{-1}	Experimental
$\sigma_{(no\ separator)}$	63 mS cm^{-1}	Experimental

Reference

1. Wang, J., Polleux J, Lim J, Dunn B. Pseudocapacitive Contributions to Electrochemical Energy Storage in TiO_2 (Anatase) Nanoparticles. *The Journal of Physical Chemistry C* **111**, 14925-14931 (2007).
2. Mo, F.*, et al.* A flexible rechargeable aqueous zinc manganese-dioxide battery working at −20 °C. *Energy & Environmental Science* **12**, 706-715 (2019).
3. Mo, F.*, et al.* Zwitterionic Sulfobetaine Hydrogel Electrolyte Building Separated Positive/Negative Ion Migration Channels for Aqueous Zn-MnO2 Batteries with Superior Rate Capabilities. *Advanced Energy Materials* **10**, 2000035 (2020).
4. Song, Z.*, et al.* A Rechargeable Zn-Air Battery with High Energy Efficiency and Long Life Enabled by a Highly Water-Retentive Gel Electrolyte with Reaction Modifier. *Adv Mater* **32**, e1908127 (2020).
5. Sun, N., Lu, F., Yu, Y., Su, L., Gao, X., Zheng, L. Alkaline Double-Network Hydrogels with High Conductivities, Superior Mechanical Performances, and Antifreezing Properties for Solid-State Zinc-Air Batteries. *ACS Appl Mater Interfaces* **12**, 11778-11788 (2020).
6. Li, H.*, et al.* Waterproof and Tailorable Elastic Rechargeable Yarn Zinc Ion Batteries by a Cross-Linked Polyacrylamide Electrolyte. *ACS Nano* **12**, 3140-3148 (2018).
7. Li, H. F.*, et al.* An extremely safe and wearable solid-state zinc ion battery based on a hierarchical structured polymer electrolyte. *Energy & Environmental Science* **11**, 941-951 (2018).
8. Zhao, J.*, et al.* A Smart Flexible Zinc Battery with Cooling Recovery Ability.

Angew Chem Int Ed Engl **56**, 7871-7875 (2017).

9. Liu, M.*, et al.* Artificial Solid-Electrolyte Interface Facilitating Dendrite-Free Zinc Metal Anodes via Nanowetting Effect. *ACS Appl Mater Interfaces* **11**, 32046-32051 (2019).
10. Yang, H.*, et al.* Constructing a Super-Saturated Electrolyte Front Surface for Stable Rechargeable Aqueous Zinc Batteries. *Angew Chem Int Ed Engl* **59**, 9377-9381 (2020).
11. Zhao, Z. M.*, et al.* Long-life and deeply rechargeable aqueous Zn anodes enabled by a multifunctional brightener-inspired interphase. *Energy & Environmental Science* **12**, 1938-1949 (2019).
12. Liang, P.*, et al.* Highly Reversible Zn Anode Enabled by Controllable Formation of Nucleation Sites for Zn-Based Batteries. *Advanced Functional Materials* **30**, 1908528 (2020).
13. Hao, J.*, et al.* An In-Depth Study of Zn Metal Surface Chemistry for Advanced Aqueous Zn-Ion Batteries. *Adv Mater* **32**, e2003021 (2020).
14 Leng, K., et al. A Safe Polyzwitterionic Hydrogel Electrolyte for Long-Life Quasi-Solid State Zinc Metal Batteries. *Adv Funct Mater* **30**, 2001317 (2020)
15 Hu, K., et al. Stabilizing zinc metal anodes by artificial solid electrolyte interphase through a surface ion-exchanging strategy. *Chemical Engineering Journal* **396**, 125363 (2020)